Università degli Studi di Padova

Dipartimento di Fisica e Astronomia "Galileo Galilei"
Corso di Laurea Triennale in Fisica

Characterization of new point contact germanium detectors for the GERDA experiment

Laureando:
Giorgio Cartechini
Matricola: **1099047**

Relatore:
Alberto Garfagnini
Correlatore:
Katharina von Sturm

Anno Accademico 2016-2017

Contents

Introduction

High-Purity Germanium (HPGe) detectors are the core of the GERDA (GERmanium Detector Array) experiment which is searching for neutrinoless double beta ($0\nu\beta\beta$) decay in the ^{76}Ge isotope at Gran Sasso.

In this thesis we will characterize a Broad Energy Germanium (BEGe) detector finding the main operational parameters: reverse-bias depletion voltage and Dead Layer (DL) [1]; a description of the standard method used to characterize germanium detectors will be given as well.

First of all, the specific detector working conditions including the correct applied voltage at which the detector is fully depleted, will be discussed. Studying the detector response to different applied High Voltage (HV), it was possible to find this parameter, an important preliminary step in order to optimize the excellent detector characteristics such as the energy resolution.

Before studying the DL parameter, the detector geometry will be verified: a precise measure of DL depends on a detailed Monte Carlo (MC) implementation of the detector geometry. Hence, thanks to an automated scanning process [2] it was possible to determine the HPGe dimensions and its holder geometry.

We will determine, also, the detector dead volume, i.e. detector region where BEGe is not sensible to energy loss by ionizing radiation: The method used to measure this parameter is based on the comparison between the experimental dataset and the correspondent MC simulation, implementing the results obtained from the detector geometry analysis.

Chapter 1

High voltage detector dependency

The Broad Energy Germanium (BEGe) detector is a particular geometry of High Purity Germanium (HPGe) detectors; the HPGe studied here is a *p-type semiconductor diode detector*, characterized by low impurity concentration [3], thus, due to the small band gap on germanium, it can obtain a very high energy resolution.

In this chapter the first important operational parameter of the detector will be given: the reverse-bias High Voltage (HV) at which HPGe crystal is fully depleted.

First of all a brief description of the working conditions at which the detector has to be kept, will be given [4]:

- **Temperature:** Germanium detectors must be cooled at the temperature of liquid nitrogen ($\sim$ 77 K), both in order to maintain electrons in the valence bound reducing the leakage of current, and to avoid further Li-diffusion of the n+ electrode that would reduce its efficiency.
- **Vacuum:** The detector is placed in vacuum to avoid thermal conductivity between the germanium crystal and the external environment.
- **Depletion voltage:** As for a common semiconductor detector, applying a specific reverse-bias voltage to the crystal, it can be maximally depleted of free charge carriers. This area corresponds to the detector active volume, sensible to ionizing radiation [1].

In order to find the HV corresponding to full depletion, the detector was irradiated by a ^{60}Co open source (i.e. without collimation) applying different HV values (from 2500 V to 3600 V). Each energy spectrum at different voltage was analyzed focusing the attention on ^{60}Co uncalibrated peak position and energy resolution: both 1173 keV and 1332 keV peaks are fitted with a Gaussian function; then, position and energy resolution are extrapolated from the fit as the Gaussian mean value and the Gaussian square root of variance respectively (the energy resolution is calculated after an energy calibration of the spectrum).
In **Figure 1.1a, b,and c** peaks position and energy resolution are plotted as a function of

the applied reverse-bias HV: it is evident that both parameters become constant after 2800 V; in particular, as expected, the energy resolution decreases until the depletion voltage is reached, increasing the detector efficiency.

Figure 1.1d, e show the 1173 keV peak at three specific HV values [V]: 2500, 2600, 2700 before and after the energy calibration: the peak position increases and the peak width decreases for HV lower than the depletion voltage (2800 V).

We can conclude that after 2800 - 3000 V the detector is fully depleted and it works at the maximum of its efficiency.

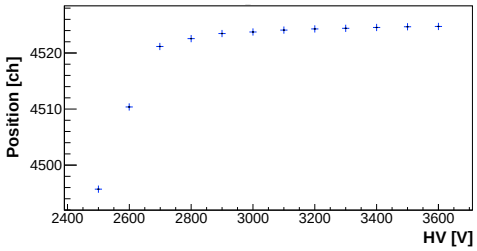

(a) ^{60}*Co 1173 keV peak position*

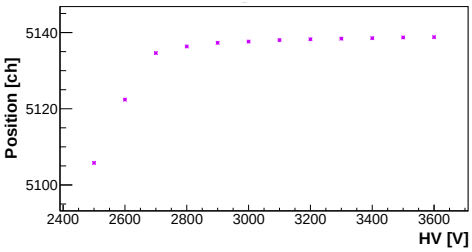

(b) ^{60}*Co 1332 keV peak position*

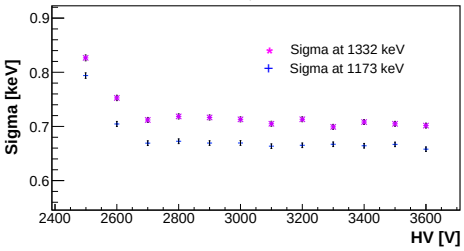

(c) ^{60}*Co peaks Energy resolution*

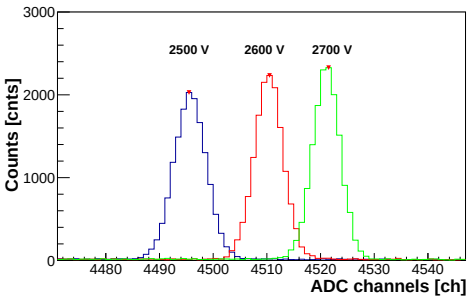

(d) *Histogram position shift of 1173 keV peak at different voltages*

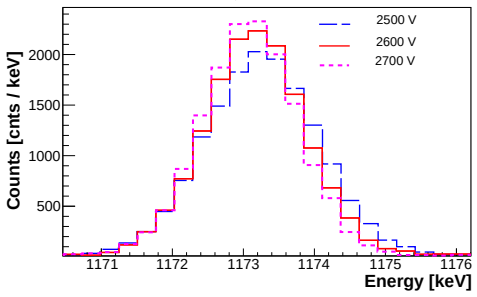

(e) *Histogram resolution decrease of 1173 keV at different voltages*

Figure 1.1: (a), (b) Peak position and detector energy resolution as function of High Voltage. (c) 1173 keV gaussian peak for three specific High Voltage values: 2500, 2600 and 2700 V. (d) The same peaks after energy calibration

Chapter 2

Detector geometry

Before we can determine the Dead Layer (DL) parameter, in this chapter we will verify the detector geometry. A detailed knowledge of detector geometry will be crucial in the Monte Carlo (MC) simulation used to compute the DL and it is described in details in the next chapter.

Now a brief description of our prior hypothesis about detector dimensions and materials, that will be verified in the next sections, is given.

2.1 Detector geometry hypothesis

The whole detector, produced by *Canberra*, is composed by a dewar and a cryostat in which there are electronic components (e.g. preamplifier and cables) and a HPGe crystal. We are interested in the detector cryostat because it contains the HPGe crystal, which is the detector's BEGe active component.
Figure 2.1 shows the detector cryostat and the dewar.

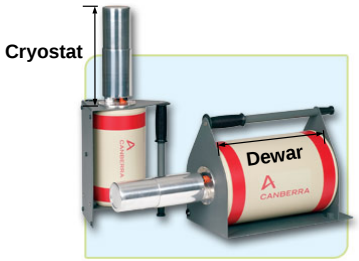

Figure 2.1: *Canberra* portable detector

The main parts of the cryostat's composition are given in the following, for more details see [5, 6].

1. **End cup**: Outer cylinder in aluminium alloy: 1.5 mm thick and with a diameter of 90 mm. On the top there is a carbon epoxy window, 0.6 mm thick. The crystal and its holder are contained inside (**Figure 2.3a, b**).

2. **Broad Energy Germanium (BEGe) detector:** The BEGe detector is composed by an HPGe crystal with a Li-diffused surface layer n+ elecrtrode and a p+ Borum-implemented electrode on the bottom. It has a height and diameter of 31 mm and 71 mm respectively; the p+ electrode is surrounded by a ditch 2 mm high and thick (**Figure 2.2a, b**).

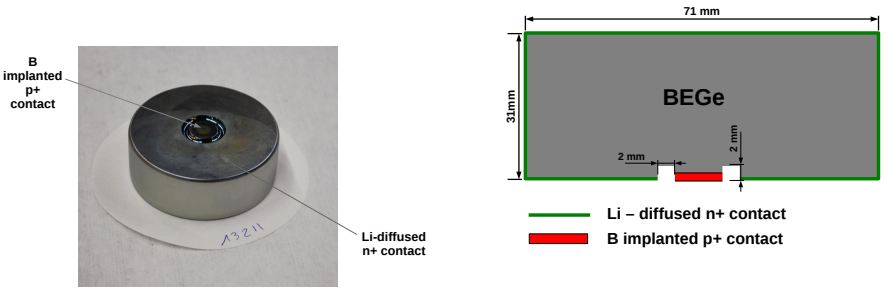

(a) *BEGe crystal 3D drawing* **(b)** *BEGe crystal 2D sketch*

Figure 2.2: (a) BEGe picture, (b) a BEGe scheme with dimensions

3. **Detector holder:** The detector is sustained in the end cap thanks to a copper holder designed by Canberra to contain one germanium crystal, thus it has an inner radius 1 mm larger than the latter. In order to maintain the BEGe stable in the cryostat there are two support rings surrounding the holder with screws to tighten the diode at its position (**Figure 2.3a, b**). The BEGe top surface is about 1 mm out of the holder.

4. **Preamplifier housing:** Part of the cryostat is situated below the detector holder and contains the detector preamplifier and cables. This part is not implemented in the Monte Carlo simulation.

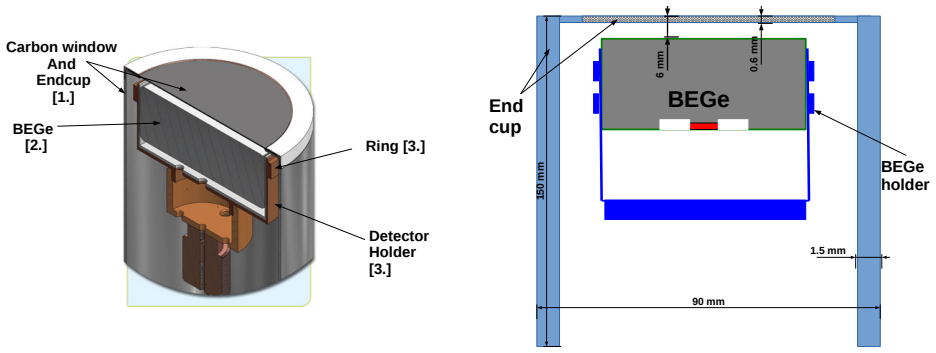

(a) *Detector cryostat 3D* **(b)** *Detector cryostat 2D sketch*

Figure 2.3: (a) Detector Cryostat 3D scheme, (b) detector cryostat 2D scheme with dimensions: 1. end cup, 2. BEGe, 3. detector holder

2.2 Geometry verification method

In order to verify the geometry described above, two detector surfaces (top and lateral) were scanned, acquiring energy spectra of an ^{241}Am collimated source. Subsequently a MC simulation was done reproducing the same experimental scan process and implementing the detector geometry characteristics shown in the previous section. From the analysis and comparison of the experimental and simulated datasets it has been possible to determine the detector geometry.

Now we give a brief description of the surfaces scan process.

Automated surfaces scan process

To study the lateral and top surface of the detector cryostat, an automated scanning table was used, designed to move a collimated source around the cryostat. The automated scanning table is built to set the source up horizontally and vertically (rotation around x axis, movement *3*), to move the source linearly along its support arm (movement *2*) and it allows the source to rotate around the z axis, parallel to the cryostat. **Figure 2.4** shows a scheme of the mechanical movements. A detailed documentation of the table is given in [2].

For the scan it was used a ^{241}Am source ($\sim$ 4310 kBq on 10/05/2017) collimated inside a copper holder of 3 cm x 3 cm x 6.5 cm dimension with a hole of 1 mm diameter.

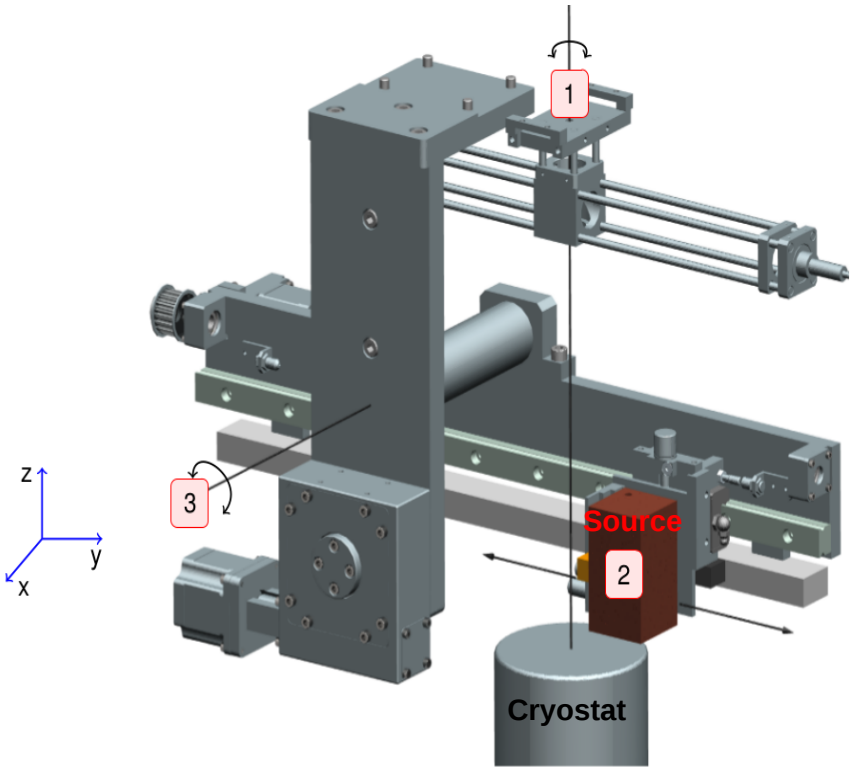

Figure 2.4: Automated scanning table and detailed mechanical movements. Taken from [2].

The cryostat lateral surface was scanned from the top to the base of the Germanium crystal using 1 mm step and rotating the source around the surface in step of 3 degrees. For the top surface, at the first, it was done a linear scan along the diameter of the detector cryostat in 1 mm step for 30s in each step (less than the lateral surface because of the carbon window) was performed to verify the correct radius. To study all the surface it was scanned from the edge to the center of the detector cryostat using steps of 5 mm and 10 degrees.

2.3 Experimental data analysis

During each scan, a Multichannel Analyzer (MCA) analyzed the signals coming from the detector preamplifier giving a histogram of frequency against energy, i.e. the energy spectrum of the ^{241}Am collimated source.
Thus, for each source position along the two surfaces, the number of detected $\gamma-$particles was calculated, extracting the number of events in the 59.95 keV peak. For that purpose, the peak was fitted using the function:

$$f(x) = p_3 + p_0 \cdot exp\left(-\frac{1}{2}\frac{(x-p_1)^2}{p_2^2}\right) + \frac{p_4 - p_3}{2} \cdot erfc\left(\frac{x-p_1}{\sqrt{2}\cdot p_2}\right) \tag{2.1}$$

which is the sum of: a constant function, a Gaussian function and the inverse error function which describes the step between the right and left tail of the Gaussian peak (p_i represents the parameters of the fit function).
The *signal* was computed as the integral of the histogram in the range $[p_1 - 3\sigma; p_1 + 3\sigma]$, where p_1 is the mean value of the Gaussian function fitted with the histogram peak and σ is the square root of the Gaussian variance i.e. p_2.
The background signal was calculated as the mean value of two backgrounds, one on the left side of the peak ($[p_1-9\sigma; p_1-3\sigma]$) and the other one on the right side ($[p_1+3\sigma; p_1+9\sigma]$) and than subtracted to the *signal*:

$$signal = events - \frac{background_{left} + background_{right}}{2} \tag{2.2}$$

Figure 2.5 shows the fit function (2.1) in red and the error Gauss function in green; the dotted lines in black delimit the three regions where the *signal* and the background are evaluated.

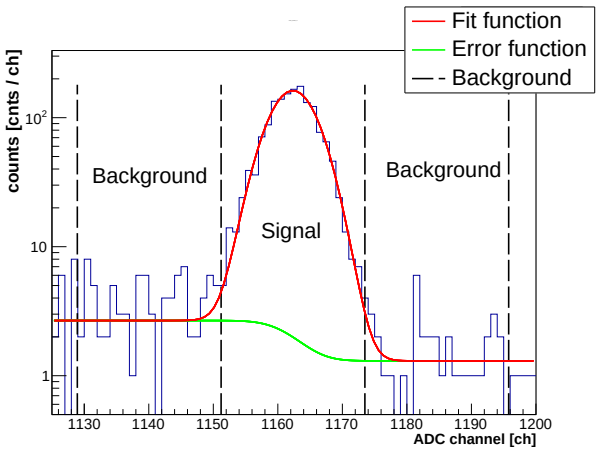

Figure 2.5: Fit function and counts ranges

Lateral surface scan results

From the lateral scan data, it is possible to deduce the geometrical structure that holds the Germanium crystal into the cryostat, thanks to the fluctuations of the *signals* along the surface caused by the ionizing radiation's attenuation through the matter. For few millimeters from the top (z = 278 mm) there is a huge signal peak constant around the surface, where the top of the Germanium crystal is outside of its holder. It is also

possible to note two regions where the *signal* is very low (z $\sim$ 290 mm and z $\sim$ 300 mm), demonstrating the fact that the detector holder is composed by two rings. As showed in **Figure 2.6**, in a restricted part of the surface there are two region where the signal counts increase considerably. Since these peaks are situated in the regions of the two holder rings, an explanation for the different count rate would be that the screws are not made of copper, but e.g. plastics to avoid electrical conductivity.

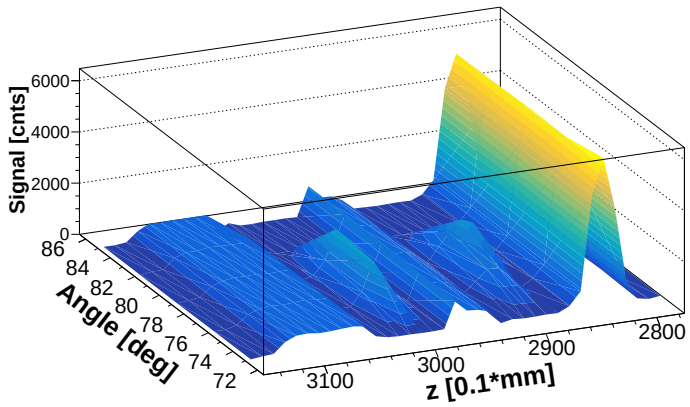

Figure 2.6: Plot of *signals* detected on the lateral surface screws' region. In the copper ring bands are visible increasing values of *signals* due to the plastic screws

Top surface scan results

Using the same method adopted for the lateral surface, data collected for the top scan shows that the BEGe detector has a homogeneous top surface. This is showed in **Figure 2.7a, 2.7b** where the signals from the top surface scan are plotted in polar coordinates. At the graph center there is a circular missing scan point due to the not perfect alignment between the scanning table and the detector cryostat center.
A more refined scan, 1 mm step size instead of 5 mm, was performed along the cryostat's diameter to verify the correct detector diameter (or radius) dimension. The result is 70.0 $\pm$ 0.5 mm (**Figure 2.7c**: the value of diameter does not correspond to the geometrical diameter of the BEGe, but to the diameter of the active volume). The systematic uncertainty associated is half step size of the source position along the arm of the automated table i.e. 0.5 mm.

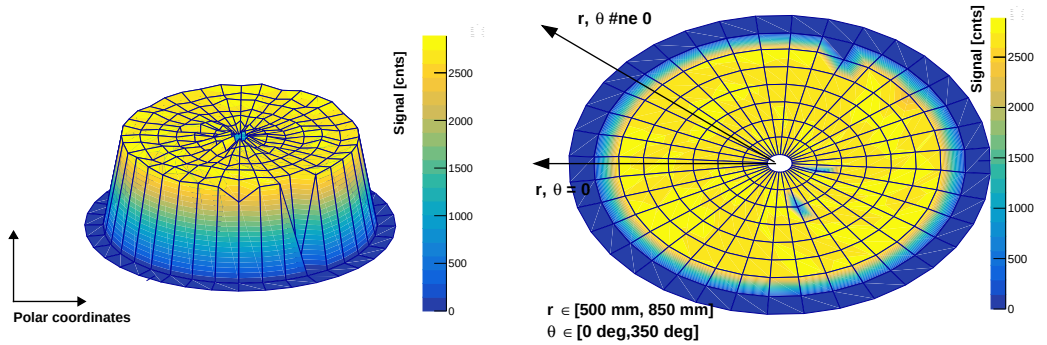

(a) *Top surface signals in polar coordinates* **(b)** *Polar coordinate on top surface*

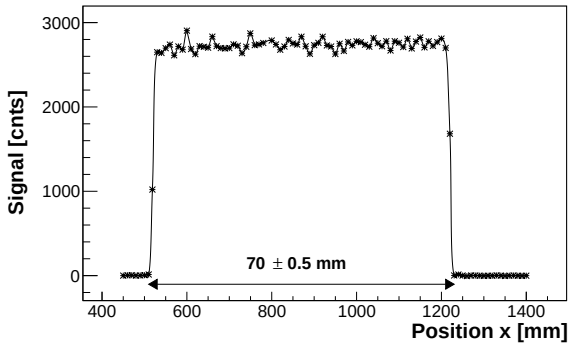

Figure 2.7: (a) and (b) Top surface scan. Below, linear scan along the cryostat' s diameter

2.4 Simulated data and comparison with experimental results

In order to verify the geometry described in the first part of this chapter (**Section 2.1**) a MC simulation was used thanks to a *Geant4* based software [7].

As for the experimental data analysis (**Section 2.3**), the peak *signals* due to ^{241}Am energy deposition were computed for the MC simulation. The method used to calculate the *signal* is different from the experimental one; in fact the MC simulation does not take into account for the detector energy resolution. For this reason the number of events has been calculated as the counts in the 59 keV bin, having subtracted the background i.e. the sum of counts in the two near bins (57 keV end 58 keV). The method is described (**Figure 2.8**).

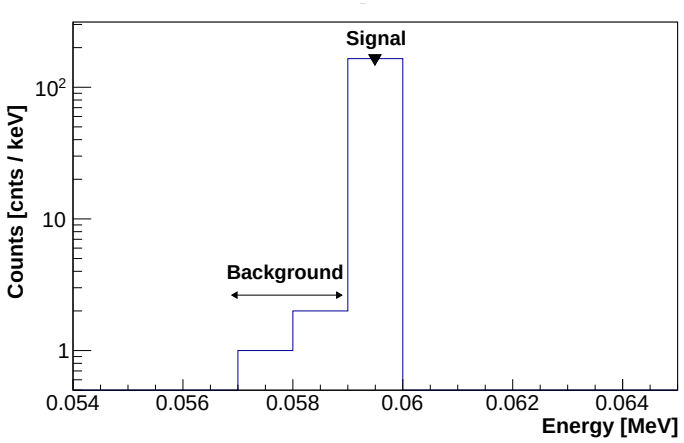

Figure 2.8: ^{241}Am simulated energy spectrum indicating signal bin and background bins

Comparison between experimental and simulated detector geometry

Comparing the results from the experimental data analysis and the simulation it is possible to verify the compatibility between the geometry implemented in the MC simulation (dimensions and materials) and the real detector geometry. In particular **Figure 2.9a** shows experimental and simulated *signals* for the top scan surface, normalized to the maximum value and we can conclude that measurements and MC data coincide within the errors. On the contrary, **Figure 2.9b** represents signals, normalized to the mean value in the rings regions (e.g. z position from 10 cm to 15 cm), detected in the lateral surface scan. From the figure two facts are evident:

A) In regions $z \in [10; 15]$ cm and $z \in [28; 37]$ cm (i.e. regions between the first and second ring, and after the second ring respectively), the simulated normalized *signals* are systematically lower than the experimental one. Thus, it is supposed that the ring thickness on MC simulation (1.5 mm) is smaller then the real one. To verify that, the experimental ring thickness is calculated from the γ-ray absorption law [8]:

$$\frac{I(d)}{I_0} = exp\left[-\frac{\mu}{\rho} \cdot x\right] = exp\left[-\frac{\mu}{\rho} \cdot \rho d\right] \tag{2.3}$$

where $I(d)$ = number of $\gamma-$ particles after the absorber thickness [cnts], I_0 = number of $\gamma-$particles before the absorber [cnts], $\frac{\mu}{\rho}$ = mass attenuation coefficient $[\frac{cm^2}{g}]$, ρ = absorber density $[\frac{g}{cm^3}]$ and d = absorber thickness $[cm]$.
From equation (2.3) the ring thickness d was computed as the *signals* ratio from the lateral scan position $z = 12$ cm ($I(d)$) and outside it (I_0), $z = 18$ cm:

$$d = \frac{1}{\mu} \cdot ln\left(\frac{I_0}{I(d)}\right) = 1.7 \pm 0.1mm \tag{2.4}$$

the attenuation coefficient $\frac{\mu}{\rho} = 1.555\ \frac{cm^2}{g}$ and the Copper density $\rho = 8.96\ \frac{g}{cm^3}$ were obtained from National Institute of Standard and Technology (NIST) XCOM [9, 10]. Thus, the ring thickness in MC simulation is probably not accurate and the *signal* systematic differences are caused by the 0.2 mm difference in ring thickness.

The uncertainty associated to equation (2.3) is calculated according to first order error propagation:

$$\sigma_d \sim \sqrt{\left(\frac{1}{I_0}\right)^2 \sigma_{I_0}^2 + \left(\frac{1}{I(d)}\right)^2 \sigma_{I(d)}^2} \tag{2.5}$$

where $\sigma_{I_0} = \sqrt{I_0}$ and $\sigma_{I(d)} = \sqrt{I(d)}$.

B) From **Figure 2.9b** is also evident that for $z \sim 6$ cm, region where the crystal is out of the holder, simulated *signals* are lower than experimental. A possible answer to this fact is that the crystal is not only 1 mm outside of the holder (as in MC simulation hypothesis) but more ($\sim$ 2 mm). This thesis is based on the grounds that the collimated $\gamma-$particles beam that irradiates the detector surfaces is not a narrow beam, but it has a conical shape; for this reason if the detector crystal is out of the holder for few millimeters more, $\gamma-$particles from the source will irradiate more crystal sensible surface and the detector will acquire more events. An other important proof is the fact that at the bottom of detector lateral surface ($z \in [35; 37]cm$) experimental *signals* goes down before the simulated one. This means that in this region the BEGe crystal is already finished, thus the experimental crystal has an higher position in the holder than in the MC simulation.

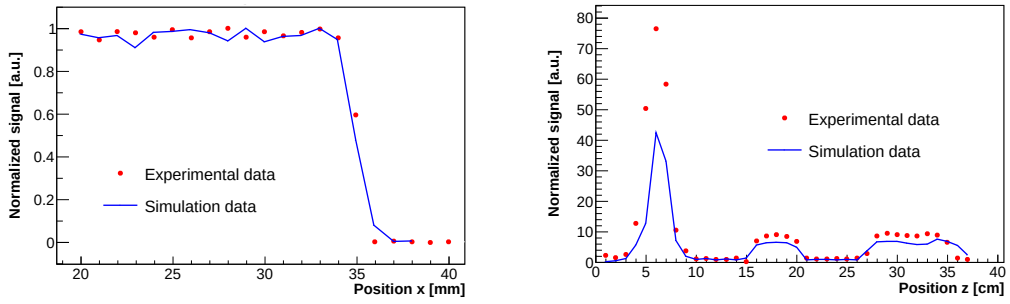

(a) *Experimental and simulated top surface scan data*

(b) *Experimental and simulated lateral surface scan data*

Figure 2.9: Comparison between data and MC. description is in the text

We can conclude that the overall geometry given by the manufacturer and implemented in MC simulation is correct, and the simulation can be corrected with a future MC simulations.

Chapter 3

Dead layer

In this chapter we use the detector geometry measured in the previous chapter to find an important operational parameter: Dead Layer (DL).

The DL is defined as the detector part from which no charges are collected; the dead layer thickness can be identified with the n+ electrode that surrounds the detector. According to the manufacturer, the BEGe has a top DL which is roughly 300 nm thick and a lateral DL about 0.1-0.5 mm (**Figure 3.1**).

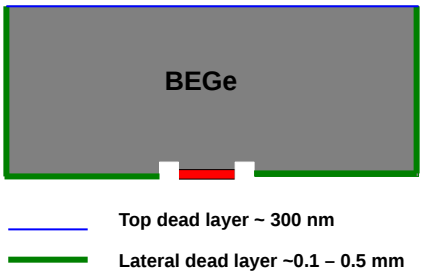

Figure 3.1: Lateral and top dead layer on BEGe

3.1 Method

In order to estimate the DL, a MC simulation using the geometry verified in the previous chapter and with null dead layer was performed. Using different DL values, the events detected in the DL volume are excluded from the simulated energy spectrum. Thus, we obtain one spectrum for each DL value. Finally, the simulated data are compared to the experimental data in order to match the DL parameter.

The comparison of simulated to experimental data is given below.

'peak count rate ratio' method with ^{241}Am source

The 'peak count rate ratio' method with ^{241}Am source is based on the determination of the peak count rate ratio parameter, $\rho(^{241}Am)$, i.e. the ratio between the number of events under the americium full energy peaks, n(E). Two ratio ^{241}Am parameters are calculated [11]:

$$\rho_{60}(^{241}Am) = \frac{n(59.5keV)}{n(99keV) + n(103keV)} \tag{3.1}$$

$$\rho_{26}(^{241}Am) = \frac{n(26keV)}{n(99keV) + n(103keV)} \tag{3.2}$$

Using the spectra constructed before (see **Section 3.1**) we obtain one ratio for ρ_{simul} for each dead layer value. The DL is determined when the simulated and measured peak count ratios are equal.

In the following we describe in details the computation of ρ_{exp} and ρ_{simul}.

Importance of ^{241}Am source

We selected an ^{241}Am source because the low energetic $\gamma-$particles at 26 keV and 59.5 keV are attenuated in the first BEGe detector layers. Instead, the two full energy peaks at 99 keV and 103 keV are absorbed deeper inside the detector. Thus, ρ is sensitive to the DL parameter.
Figure 3.2 shows the number of hits in the detector volume: it is evident that using this particular source located above the detector top, the method is sensitive only to the top dead layer.

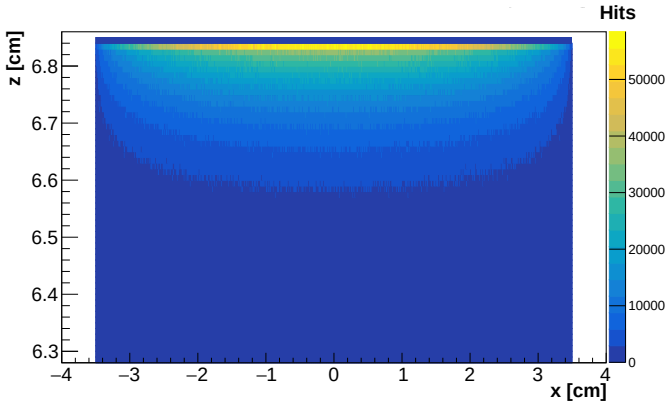

Figure 3.2: The number of $\gamma-$particle hits in the detector active volume from MC simulation (DL = 0 mm)

3.2 Experimental peak count rate ratio ρ_{exp}:

At first an energy spectrum was taken using an uncollimated ^{241}Am source (activity: 371 ± 3 % kBq on 21/06/2017), located at 254.4 mm from the carbon window on the top of cryostat. To calculate the peak count rate n(E), the energy spectrum was calibrated and each $\gamma-$peak fitted with the following functions:

$$f_1(x) = f_2(x) + \frac{p_4 - p_3}{2} \cdot erfc\left(\frac{x - p_1}{\sqrt{2} \cdot p_2}\right) \tag{3.3}$$

$$f_2(x) = p_3 + p_0 \cdot exp\left(-\frac{1}{2}\frac{(x - p_1)^2}{p_2^2}\right) \tag{3.4}$$

The function (3.3), sum of three functions: a) constant function, b) Gauss function and c) inverse error function, was used to fit the 59.5 keV and 26 keV peaks; the function (3.4), equal to $f_1(x)$ but without inverse error function background approximation, for 99 keV and 103 keV peaks. n(E) (E=26, 59.5, 99 and 103 keV) is calculated as the integral of Gaussian fit function without the background (constant and inverse error function) in the range [p_1 - 5p_2; p_1 + 5p_2] (where p_1 and p_2 correspond to the Gaussian mean and the square root of variance σ respectively). In **Figure 3.3** there is an example of the peak fit functions $f_1(x)$ and $f_2(x)$.

3.3 Simulated peak count rate ratio ρ_{simul}:

The MC simulation (**Section 3.1**) does not take the detector resolution into account which gives the typical Gaussian shape to γ-lines in spectra. In order to recreate the same Gaussian shape of the experimental spectrum a *smearing* in energy was applied, i.e. random numbers from a Gaussian distribution were generated with null *mean* and *experimental square root of variance* ($\mu = 0$, $\sigma = \sigma_{exp}$) and added to the energy deposited inside the detector. **Figure 3.4** shows a simulated energy spectrum before and after smearing.

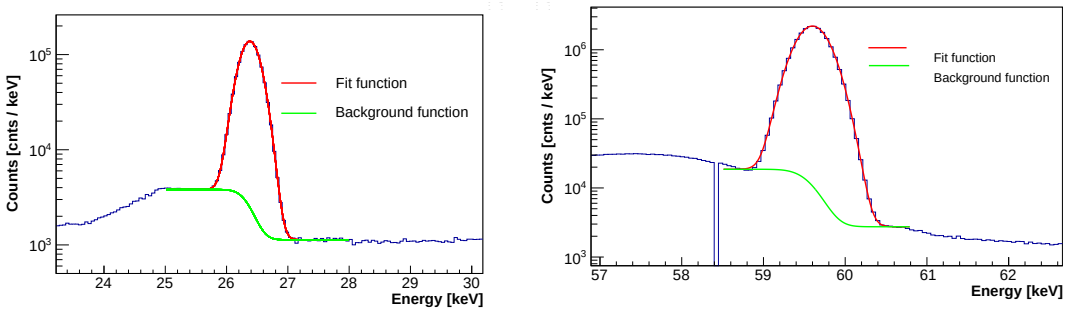

(a) *Peak at 26 keV fit with* $f_1(x)$ **(b)** *Peak at 59.5 keV fit with* $f_1(x)$

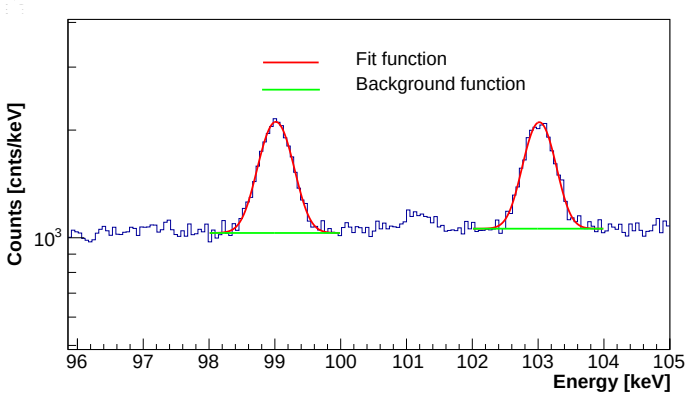

Figure 3.3: Fit function (*red*) and background function (*green*) in ^{241}Am energy spectrum

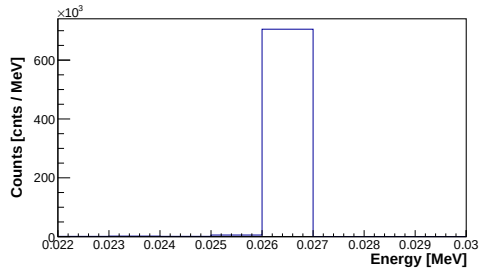

(a) ^{241}*Am peak at 26 keV without smearing technique*

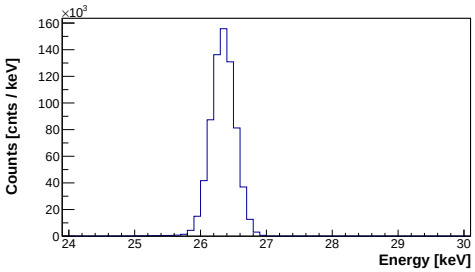

(b) ^{241}*Am peak at 26 keV with smearing technique*

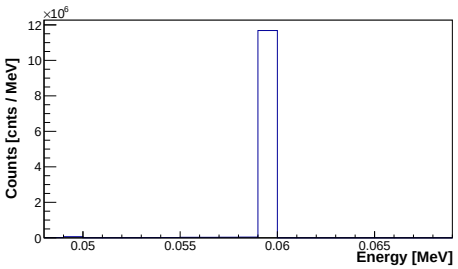

(c) ^{241}*Am peak at 59.5 keV without smearing technique*

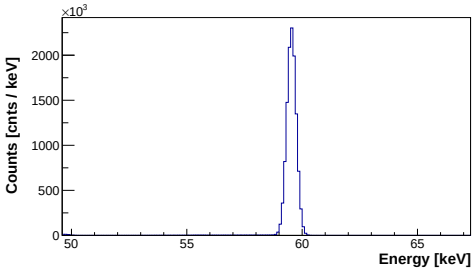

(d) ^{241}*Am peak at 59.5 keV with smearing technique*

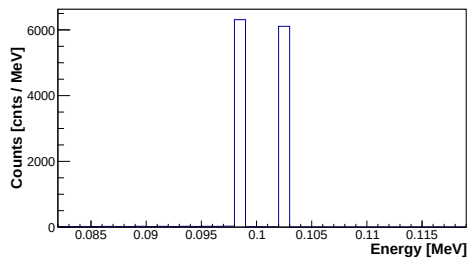

(e) ^{241}*Am peaks at 99 keV and 103 keV without smearing*

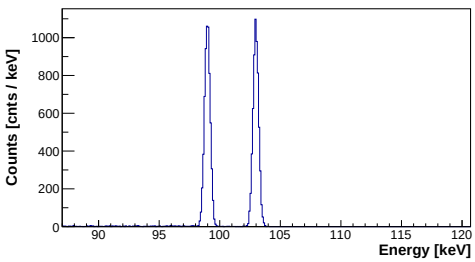

(f) ^{241}*Am peaks at 99 keV and 103 keV with smearing*

Figure 3.4: Difference between energy spectra (a), (c), (d) without smearing, (b), (d), (f) with smearing

To calculate the quantity n(E) in equation (3.1) and (3.2), each γ-peak in simulated energy spectrum was fitted with functions (3.3) and (3.4) and calculated their integrals in range [p_1 - $5p_2$; p_1 + $5p_2$] subtracting the background, as in the experimental data.

This method was repeated for each simulated energy spectrum at different DL values, obtaining a sequence of peak count rate ratio parameters. **Figure 3.5** shows that the number of events under the 59.59 keV peak decreases at increasing DL values due to the exclusion of events in dead layer volume. Thus, the detector is very sensible to the ^{241}Am $\gamma-$particles detected in DL range, as explained in previous section.

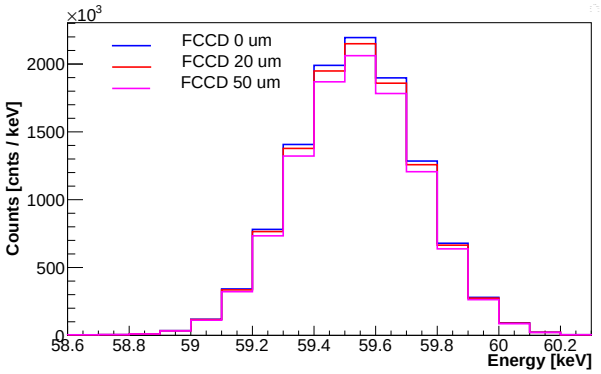

Figure 3.5: ^{241}Am peak at 59.5 keV using three values of DL thickness: *Blue* 0 μm, *Red* 20 μm, *Green* 50 μm

3.4 DL parameter extraction from ρ_{exp} and ρ_{simul}

After having calculated the quantity $\rho(^{241}Am)$ for both experimental data and simulation $\rho_{simul}(^{241}Am)$ was fitted as a function of DL value with a cubic function:

$$f(x) = p_0 + p_1 \cdot x + p_2 \cdot x^2 + p_3 \cdot x^3 \tag{3.5}$$

The measured peak count rate ratio was added to the plot and the intersection point between the latter and the fit function (3.5) determines the dead layer thickness of BEGe detector. **Figure 3.6a, b** represents the graph with the cubic function fitting 59.5 keV and 26 keV peak ratios and the constant function linked to ρ_{exp} from experimental analysis:

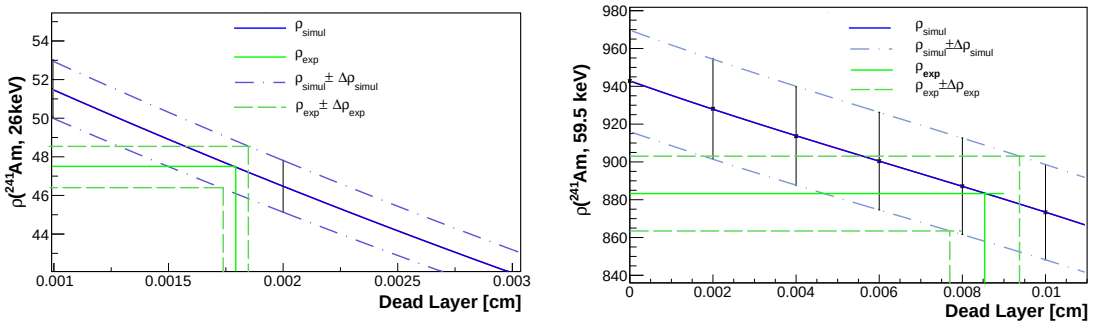

(a) *Dead Layer extraction value from ρ_{exp} and ρ_{simul} of 26 keV peak*

(b) *Dead Layer extraction value from ρ_{exp} and ρ_{simul} of 59.5 keV peak*

Figure 3.6: (a) Extraction of DL value comparing the experimental peak count rate ratio to the simulation, using (a) the 26 keV peak and (b) the 59 keV peak

3.5 DL determination from $\gamma-$ray absorption law

The DL was determined from the $\gamma-$ray absorption law (equation (2.3)) discussed in the previous chapter: using the experimental data acquired for the lateral and top surface scans (**Section 2.3**), the ratio between the number of events in the 59.5 keV ^{241}Am peak detected in the detector lateral surface ($z \in [15; 20]$ cm in **Figure 2.9a**) and the *signals* in the top surface (**Figure 2.9a**) was calculated.

Thus, assuming the DL on the top surface is much less than the lateral, the DL parameter is calculated as follows [8, 9]:

$$\frac{I^{lat}}{I^{top}} = \frac{I_0 \cdot t^{lat}}{I_0 \cdot t^{top}} \cdot \frac{exp(-\mu^{lat} d^{lat})}{exp(-\mu^{top} d^{top})} \tag{3.6}$$

where I_0 is the source activity, t is the measurements live time, $\mu^{lat} d^{lat} = \mu^{cryo} d^{cryo} + \mu^{holder} d^{holder} + \mu^{Ge} \cdot x$, the sum of attenuation coefficients of alluminium cryostat, copper holder and germanium (x = DL), and μ^{top} is the attenuation coefficient of the Carbon epoxy window (density 2.3 $\frac{g}{cm^3}$; composition 71.5% C, 12.6% H, 15.9% O). Hence, we obtain:

$$x = DL = \frac{1}{\mu^{Ge}} \cdot \left(\mu^{top} d^{top} - \mu^{cryo} d^{cryo} - \mu^{holder} d^{holder} - ln\left[\frac{I^{lat} \cdot t^{top}}{I^{top} \cdot t^{lat}} \right] \right) \tag{3.7}$$

3.6 Uncertainty estimation

- **Peak count rate uncertainty $\sigma_{n(E)}$:** a statistic uncertainty as square root of count rates i.e. $\sigma_{n(E)} = \sqrt{n(E)}$ was associated.

- **Peak count rate ratio uncertainty σ_ρ:** According to the equations (3.1), (3.2), it was associated to the quantity $\rho(^{241}Am)$ an uncertainty calculated by the error propagation (E=26 keV and 59.5 keV):

$$\sigma_{n(E)} \sim \sqrt{n(E)}$$

$$\sigma_+ = \sigma_{n(99keV)+n(103keV)} \sim \sqrt{n(99keV)^2 + n(103keV)^2}$$

$$\sigma_\rho \sim \sqrt{\left(\frac{1}{n(99keV)+n(103keV)}\right)^2 \sigma^2_{n(E)} + \left(\frac{n(E)}{(n(99keV)+n(103keV))^2}\right)^2 \sigma^2_{\sigma_+}}$$

- **DL uncertainty 'peak count rate ratio' method:** The uncertainty associated to the DL value was estimated as the intersection between the fit function f(x±Δx) ($x \pm \Delta x = \rho_{simul} \pm \sigma_{\rho_{simul}}$) and the constant functions $\rho_{exp} \pm \sigma_{\rho_{exp}}$. **Figure 3.6** shows the uncertainty range bounded by green dotted lines.

- **DL uncertainty $\gamma-$ray absorption law:** To the DL measure in equation (3.7) we associate a statistic uncertainty derived by the error propagation:

$$\sigma_{DL} \sim \sqrt{\left(\frac{1}{I^{lat}}\right)^2 \sigma^2_{I^{lat}} + \left(\frac{1}{I^{top}}\right)^2 \sigma^2_{I^{top}}} \tag{3.8}$$

Systematic uncertainty

Holder thickness The uncertainty of the copper holder thickness was estimated as ±0.1 mm [11]. Thus, taking d^{holder} as 1.6 mm instead of 1.5 mm, the DL calculated from equation (3.7) is: DL(d^{holder} = 1.6 mm) = 0.42 ± 0.04 mm. We can conclude that the systematic due to the holder is roughly 25%.

Top dead layer thickness In **Section 3.5** we have ignored the top dead layer because it is much smaller than the lateral one. Including it in the equation (3.7) (i.e. $\mu^{top}d^{top} = \mu^{window}d^{windw} + \mu^{Ge} \cdot 300$ nm), the result does not change according to the statistic uncertainty. Therefore, we do not associate an uncertainty due to the top DL thickness.

Carbon epoxy window thickness The systematic uncertainty associated to the carbon epoxy window thickness was taken as ±0.1 mm. MC simulations were performed using

0.7 mm of carbon window thickness instead of 0.6 mm: we calculate $DL_{26} = 17.4^{+0.5}_{-0.6}$ μm and $DL_{60} = 78^{+7}_{-8}$ μm. Thus, the systematic uncertainty for the carbon window thickness is about 2% for DL_{26} and 7% for DL_{60}.

Top and lateral DL values

Using the 'peak count rate ratio method' we have obtained two different top DL values:

- $DL_{26} = 17.9^{+0.5}_{-0.6}$ μm (stat.) ± 0.5 μm (sys.)
- $DL_{60} = 85 \pm 8$ μm (stat.) ± 6 μm (sys.)

Instead, from the $\gamma-$ray absorption law we have calculated the lateral DL:

- $DL = 0.56 \pm 0.4$ mm (stat.) ± 0.8 mm (sys.)

Chapter 4

Discussion and Conclusion

High voltage

In the first chapter we have studied the detector dependency on the revers-bias high voltage: we can conclude that the detector is fully depleted at 2800 V, reaching a very high energy resolution: 1.66 ± 0.02 keV @ 1332 keV (Full Width Half Maximum) (see **Figure 1.1b**).

Detector Geometry

A quite good correspondence between the implemented geometry in MC simulation and experimental data was found. Only two aspects are still open about lateral surface: the detector support ring thickness implemented in simulation (1.5 mm) does not correspond to the one calculated from experimental data: 1.7 ± 0.1 mm (**Section 2.4**); the BEGe crystal portion which is outside of the holder is probably more than 1 mm as is implemented in MC simulation. Evidences are the low count rate in MC simulation where the detector is outside the holder and the misalignment of experimental and simulated data at the bottom of the detector.

These two aspects could be verified with a slightly modified MC simulation. Despite that, we can conclude that the detector and holder geometry matches the one given by the manufacturer.

Dead Layer

The n+ electrode is divided in three layers: Dead Layer, Transition Layer (TL) where only part of charges are collected and below the TL there is the Fully Active Volume (FAV) where all charges are collected. The sum of DL an TL is called Full Charge Collection Depth.

The analysis performed in the previous chapter does not implement the TL, thus in first approximation we have assumed FCCD $\sim$ DL. An improvement of this method can be the TL modeling.

Top Dead Layer

Comparing the results from the 'peak count rate ratio method' with the top dead layer value taken from the constructor characteristics, there is a tension between the manufacturer value and the DL values deduced by both ratio methods:

- *DL top surface from manufacturer* $\sim$ 300 nm
- $DL_{26} = 17.9^{+0.5}_{-0.6}$ μm (stat.) ± 0.5 μm (sys.)
- $DL_{60} = 85 \pm 8$ μm (stat.) ± 6 μm (sys.)

We suspect that, using an ^{241}Am open source located at the top of detector, we are sensitive only to the top surface dead layer and, due to systematics uncertainties, we do not reach the sensitivity of dead layer thickness. There are several hypothesis about systematic uncertainties that affect the DL measure: first of all the implemented carbon epoxy window composition (71.5% C, 12.6% H, 15.9% O) can be different from the real one; on the detector corners the electric field is very law, thus, not all charges drifts to the electrodes increasing the FCCD area. The MC simulation, also, can not be sensitive to the *nm* thickness order and during the comparison process systematics uncertainties overestimate the measure.

In order to improve the peak count rate ratio method, experimental data could be acquired from a collimated source (e.g. ^{241}Am or ^{133}Ba) obtaining a higher sensitivity on the top dead layer surface thanks to the accurate knowledge about the scanning region.

Lateral Dead Layer

From the $\gamma-$ray absorption law we have found a DL measure compatible with the one given by the manufacturer within the uncertainty:

- *DL from manufacturer* $\sim$ 0 - 0.5 mm.
- *DL from absorption law* $= 0.56 \pm 0.4$ mm (stat.) ± 0.8 mm (sys.)

The DL value from the manufacturer is only the order of magnitude of the real one, in fact the n+ electrode thickness is always increasing due to the detector thermal conditions.

The lateral dead layer measure can be improved acquiring not only the full energy peak at 59 keV but also at 26 keV and 103 keV (collimated ^{241}Am source), in order to apply the 'peak count rate ratio' method and verify the lateral dead layer thickness.

Bibliography

[1] Dusan Budjáš et al. Isotopically modified ge detectors for GERDA: from production to operation. *JINST*, 8(04):P04018, 2013.

[2] E Andreotti et al. Heroica: an underground facility for the fast screening of germanium detectors. *JINST*, 8(06):P06012, 2013.

[3] Mayeen Uddin Khandaker. High purity germanium detector in gamma-ray spectrometry. *IJFPS*, 1(2):42–46, 2011.

[4] Glenn F Knoll. *Radiation detection and measurement*. John Wiley & Sons, 2010.

[5] E Andreotti et al. Full charge collection depth and active volume of gerda Phase II BEGe detectors. GERDA *scientific technical report.*, 2016.

[6] Canberra. Broad Energy Germanium Detectors (BEGe), 2017. http://www.canberra.com/products/detectors/germanium-detectors.asp. Available online on 24/08/2017, at 5:49 p.m.

[7] Katharina von Sturm. *Confined event samples using Compton coincidence measurementsfor signal and background studies in the* GERDA *experiment*. PhD thesis, University of Padova, 2016.

[8] NIST. X-ray Mass Attenuation Coefficient, 2017. https://physics.nist.gov/PhysRefData/XrayMassCoef/chap2.html. Available online on 4/09/2017, at 9:30 a.m.

[9] NIST. Nist xcom, 2017. https://physics.nist.gov/PhysRefData/Xcom/html/xcom1.html. Available online on 4/09/2017, at 9:30 a.m.

[10] NIST. Elements density, 2017. https://physics.nist.gov/PhysRefData/XrayMassCoef/tab1.html. Available online on 4/09/2017, at 9:30 a.m.

[11] Björn Lehnert. *Search for* $2\nu\beta\beta$ *Excited State Transitions and* HPG*e Characterization for Surface Events in* GERDA P*hase* II. PhD thesis, 2015.